The Cryosphere Discuss., 8, 887–918, 2014
www.the-cryosphere-discuss.net/8/887/2014/
doi:10.5194/tcd-8-887-2014

The Cryosphere Discussions
Open Access

Thermal resistances in the Everest Area (Nepal Himalaya) derived from satellite imagery using a nonlinear energy balance model

D. R. Rounce and D. C. McKinney

Center for Research in Water Resources, University of Texas at Austin, Austin, Texas, USA

Received: 29 December 2013 – Accepted: 14 January 2014 – Published: 27 January 2014

Correspondence to: D. R. Rounce (david.rounce@utexas.edu)

Published by Copernicus Publications on behalf of the European Geosciences Union.

Abstract

Debris thickness is an important characteristic of many debris-covered glaciers in the Everest region of the Himalayas. The debris thickness controls the melt rates of the glaciers, which has large implications for hydrologic models, the glaciers response to climate change, and the development of glacial lakes. Despite its importance, there is little knowledge of how the debris thickness varies over these glaciers. This paper uses an energy balance model in conjunction with Landsat7 ETM+ satellite imagery to derive thermal resistances, which is the debris thickness divided by the thermal conductivity. The developed model accounts for the nonlinear temperature gradient in the debris cover to derive accurate thermal resistances. Fieldwork performed on Lhotse Shar/Imja glacier in September 2013 was used to validate the satellite-derived thermal resistances. Results indicate that accounting for the nonlinear temperature gradient is crucial. Furthermore, correcting the incoming shortwave radiation term for the effects of topography and including the turbulent heat fluxes is imperative to derive accurate thermal resistances. Since the topographic correction is important, the model will improve with the quality of the DEM. The main limitation of this work is the poor resolution (60 m) of the satellite's thermal band. The derived thermal resistances are accurate at this resolution, but are unable to derive trends related to slope and aspect on a finer scale. Nonetheless, the study finds this model derives accurate thermal resistances on this scale and is transferable to other debris-covered glaciers in the Everest region.

1 Introduction

Debris-covered glaciers are common in the Everest area of the Himalayas. The debris cover has a large impact on the sub-debris ablation rate and hence the evolution of the glacier. A thin debris layer may enhance ablation by reducing the albedo causing the surface to absorb more radiation compared to clean ice, while a thicker debris layer will

TCD
8, 887–918, 2014

insulate the glacier causing the ablation rate to decrease. The critical thickness at which the debris cover reduces ablation is around 2 cm (Ostrem, 1959; Mattson et al., 1993; Kayastha et al., 2000). Field studies have supported these results showing that beyond this critical thickness, the melt rate greatly decreases (Nakawo and Young, 1981; Conway and Rasmussen, 2000; Nicholson and Benn, 2006; Reid and Brock, 2010; Reid et al., 2012). The role that debris cover has on the evolution of glaciers in the Everest area is summarized well by Benn et al. (2012). In short, the debris cover increases towards the tongue of the glacier, where the slopes are gentler. The spatial variation of debris cover causes the ablation to be predominately focused in areas of thinner debris behind the tongue of the glacier. The differential melting causes the tongue of the glacier to become stagnant and promotes the development of supraglacial lakes.

The sub-debris ablation rate is controlled by the debris thickness, the thermal properties of the debris, and meteorological conditions. The debris thickness may be measured by surveying exposed ice faces (Nicholson and Benn, 2012) or via manual excavation (Reid et al., 2012). Surveying exposed ice faces greatly reduces the amount of labor involved in measuring the debris thickness, but may not be representative of the entire glacier and is limited to regions with significant differential melting. Due to the labor-intensive nature of this work, few other surveys of debris thickness have been performed in the Everest area (Nakawo et al., 1986). The thermal property associated with describing the debris cover is the effective thermal conductivity. Studies have found the thermal conductivity of debris cover in the Khumbu to range from 0.85 to 1.29 $\mathrm{W\,m^{-1}\,K^{-1}}$ (Conway and Rasmussen, 2000; Nicholson and Benn, 2012). The water content and lithology of the debris cover may partly explain the variation in thermal conductivity as the water content will change the effective thermal conductivity of the debris (Nicholson and Benn, 2006) and the lithology will influence the bulk volumetric heat capacity, which is used to derive the thermal conductivity (Nicholson and Benn, 2012).

In addition to the properties of the debris cover, the meteorological conditions will affect the sub-debris ablation rate. The net solar radiation has been found to be the

TCD
8, 887–918, 2014

main source of energy responsible for ablation on debris-covered glaciers (Inoue and Yoshida, 1980; Kayastha et al., 2000; Takeuchi et al., 2000); however, the turbulent heat fluxes are still significant (Brock et al., 2010). Many studies have modeled the energy balance on debris-covered glaciers with varying levels of success (Nakawo and Young, 1982; Nakawo et al., 1999; Han et al., 2006; Nicholson and Benn, 2006; Mihalcea et al., 2008b; Reid and Brock, 2010; Reid et al., 2012). These models integrate meteorological data from automatic weather stations with knowledge of the debris cover to solve for the surface temperature of the debris, which may then be used to calculate the sub-debris ablation rates. These models are limited by their knowledge of how the debris cover varies over the glacier or they require a great deal of site-specific information.

This has led other studies to use satellite imagery to derive the properties of the debris cover. These studies use surface temperature data from Aster or Landsat satellite imagery in conjunction with an energy balance model to solve for the thermal resistance, which is the debris thickness divided by the thermal conductivity (Nakawo and Rana, 1999; Nakawo et al., 1999; Suzuki et al., 2007; Zhang et al., 2011). If the thermal conductivity of the debris is known, the model can solve directly for debris thickness (Foster et al., 2012). Mihalcea et al. (2008a) used a different approach by deriving debris thickness from linear relationships between surface temperature and debris thickness for different elevation bands.

One problem associated with the studies that solved for the thermal resistance is that while the spatial distribution of thermal resistances typically agreed well, the actual values of thermal resistances were significantly lower than those derived from field studies. Suzuki et al. (2007) attributed their low thermal resistances to the mixed pixel effect, which refers to the pixels in the satellite imagery comprising supraglacial ponds, ice cliffs, and bare ice areas. Nakawo and Rana (1999) also commented on areas with exposed ice cliffs reducing the surface temperature of the pixel, thereby lowering the calculated thermal resistances. Zhang et al. (2011) did not address the low values of thermal resistances, but did attribute the small disagreement between modeled and observed melt rates to the unknown variations in meteorological conditions caused by

TCD
8, 887–918, 2014

altitude, aspect, and shading in different areas, as well as the unknown nature of water content in the debris. The mixed pixel effect and the spatial variation in meteorological conditions may reduce the thermal resistances, but it is unlikely to cause the satellite-derived thermal resistances to be one or two orders of a magnitude lower than those found in the field.

Foster et al. (2012) is the first study, to the authors' knowledge, that accurately derives debris thickness from satellite imagery. The model uses a DEM generated from an airborne lidar survey and compares the results of a sloped model, which accounts for variations in topography, and a flat model. The sloped model resulted in thicker debris areas when compared to the flat model, but also identified some pixels as having unrealistically high or negative debris thicknesses. These errors occurred in pixels with steep slopes and high surface temperatures and were replaced with the values from the flat model. Unfortunately, the model is difficult to transfer to other glaciers because a great deal of site-specific data was used. Their modifications to their energy balance include the addition of a heat storage term that is a fraction of the ground heat flux and an empirical relationship between the surface temperature and air temperature.

We report a method for deriving the thermal resistances of debris-covered glaciers using an energy balance model with Landsat7 ETM+ satellite imagery and apply the method in the Everest region of Nepal. The performance of various models is assessed via comparison with field data. First, the use of a correction factor that accounts for the nonlinear temperature gradient in the debris cover is investigated. This simple nonlinear energy balance model is then used to compare a flat model with a sloped model, which accounts for the variations in topography. The affect of the quality of the DEM is then explored by comparing DEMs of different resolutions. Lastly, the applicability of this model to other areas is discussed.

TCD
8, 887–918, 2014

2 Data

2.1 Meteorological data

The energy balance model uses meteorological data from an automatic weather station, Pyramid Station (27.959° N, 86.813° E, 5035 m a.s.l). Pyramid Station (SHARE network operated by EV-K^2-CNR Committee) provides a continuous record of hourly measurements of air temperature, relative humidity, wind speed, incoming shortwave radiation, and incoming longwave radiation from October 2002 to December 2009.

2.2 Remotely sensed data

Landsat7 ETM+ (hereon referred to as Landsat7) satellite imagery over the same period as the meteorological data was used to derive the thermal resistance of the debris. All clear-sky images from the same period of time that meteorological data are available in the melt season were used. The melt season was defined as 15 May to 15 October, which is the time period where the temperature in the debris was above freezing (Nicholson, 2005). Twelve Landsat7 images met this criterion (Table 1). All scenes were downloaded from the NASA Land Processes Distributed Active Archive Center (NASA LP DAAC, 2011).

The processing level of the Landsat7 images were all L1T indicating the images were all geometrically rectified using ground control points (GCPs) from the 2005 Global Land Survey in conjunction with the 90 m global DEM generated by the Shuttle Radar Topographic Mission (SRTM). Landsat7 satellite imagery comprises 8 different bandwidths with various resolutions. The two bands of interest here are the thermal band (Band 6) and the panchromatic band (Band 8). The thermal band has a resolution of 60 m, but is automatically resampled to 30 m and was used to derive surface temperature according to NASA (2011). It was atmospherically corrected using the methods described by Coll et al. (2010). The required meteorological data for the MODTRAN 4 model used by Coll et al. (2010) was taken from Pyramid Station. The image-to-image

TCD
8, 887–918, 2014

co-registration for Landsat7 is 7.3 m and the uncertainty of the derived surface temperature data is estimated to be ±1.0 K (Barsi et al., 2003; Coll et al., 2010, 2012). The panchromatic band has a horizontal resolution of 15 m and was used to co-register the images.

The high resolution DEM used in this study was generated by Lamsal et al. (2011) from Advanced Land Observing Satellite (ALOS) PRISM images. The generated DEM has a horizontal resolution of 5 m and relative error of ±4 m. In order to co-register the DEM with the panchromatic band from the Landsat7 imagery, a shaded version of the DEM was generated using the Hillshade tool in ArcGIS 10.3. The swipe visualization tool in PCI Geomatica 2013 showed that the images were properly co-registered without any further processing. The coarser resolution global DEM used in this study was the ASTER GDEM, which is composed of automatically generated DEMs from the Advanced Spaceborne Emission and Reflection radiometer (ASTER) stereo scenes acquired from 2000-present (METI/NASA/USGS, 2009). Nuth and Kaab (2011) found the accuracy of the ASTER GDEM to be similar to the validation summary (METI/NASA/USGS, 2009) when applied to debris-covered glaciers in New Zealand. They found the ASTER GDEM to have biases up to 10 m and RMSE of 5–50 m. The horizontal resolution of the ASTER GDEM has been found to be better than 50 m (Fujisada et al., 2005). The swipe visualization tool in PCI Geomatica 2013 was used with a shaded version of the ASTER GDEM to confirm that the images were properly co-registered. While residual anomalies and artifacts may exist in this experimental/research grade product, it has been used in this study to develop an understanding of how the quality of DEM will affect the thermal resistances.

2.3 Field data

Field research was conducted in September 2013 on the debris-covered portion of Lhotse Shar/Imja glacier located behind the calving front of Imja Lake (Fig. 1). Debris thermistors (TR-52 ThermoRecorder, T&D Corporation) were installed at four locations (referred to as LT1, LT2, LT3, and LT4) at depths of 0, 5, 10, 15, 20, 30 cm, and at

TCD
8, 887–918, 2014

the debris/ice interface. Holes were excavated to the debris/ice interface and as the thermistors were installed, the debris was replaced in its original position as best as possible. The thermistors recorded temperature at hourly intervals from 13 September to 24 September. The first 48 h of data for each thermistor was discarded to allow the thermistors to equilibrate with the debris. One of the surface thermistors malfunctioned on 23 September, so the data from this thermistor beyond this date was discarded.

Debris thickness measurements were performed at 25 locations and were concentrated in one melt basin that appeared to be formed by differential melting and backwasting (Fig. 1). The melt basin was selected as the focus area of this study because it appeared to be representative of the hummocky terrain on Lhotse Shar/Imja glacier and was relatively easy to access. To the best ability of the authors, the measurements were performed randomly throughout the melt basin. Of the 25 sites, 23 were measured via manual excavation using a tape measure. This process involved digging holes to the ice surface and measuring the perpendicular distance from the ice surface to the surface of the debris. The other two sites were the debris on top of an ice face, which was measured using a laser range finder (TruPulse 360B) because the ice face could not be accessed safely on foot. Twelve debris thickness measurements were also performed outside of the melt basin to understand if the melt basin was representative of the debris-covered glacier. More debris thickness measurements were unable to be made due to time and labor restraints. Furthermore, the maximum depth of excavation was 1 m because further excavation was too physically demanding.

TCD
8, 887–918, 2014

3 Methods

3.1 Energy balance model

The energy balance model developed for the debris cover is a steady state energy balance similar to Nakawo and Young (1982)

$$R_n + H + \mathrm{LE} - Q_c = 0 \quad (1)$$

where R_n is the net radiation flux, H is the sensible heat flux, LE is the latent heat flux, and Q_c is the ground heat flux (all in $\mathrm{W\,m^{-2}}$). The control volume for this energy balance is the upper 10 cm of the debris (Fig. 2) and is assumed to be in steady state.

The net radiation flux includes the shortwave radiation flux and the longwave radiation flux

$$R_n = S\downarrow(1-\alpha) + \varepsilon(L\downarrow - \sigma T_S^4) \quad (2)$$

where $S\downarrow$ is the incoming shortwave radiation ($\mathrm{W\,m^{-2}}$), α is the albedo (0.30), ε is the emissivity (assumed to be 0.95), $L\downarrow$ is the incoming longwave radiation ($\mathrm{W\,m^{-2}}$), σ is the Stefan–Boltzmann constant ($5.67\times10^{-8}\,\mathrm{W\,m^{-2}\,K^{-4}}$), and T_S is the surface temperature (K). For the sloped model, incoming shortwave radiation was corrected for the effects of topography, altitude, and shading similar to the methods of Hock and Noetzli (1997). The flat model assumes that each pixel has a slope of 0° and does not correct for the topography. The incoming longwave radiation and surface albedo were assumed to be constant over the entire debris cover. The albedo used in this study (0.30) was the average albedo of the debris cover on Ngozumpa glacier (Nicholson and Benn, 2012).

TCD
8, 887–918, 2014

The turbulent fluxes were calculated according to Nicholson and Benn (2006) with a modification to the computation of the surface vapor pressure

$$H = \rho_{\text{air}} \left(\frac{P}{P_0} \right) c A u \left(T_{\text{air}} - T_{\text{s}} \right) \tag{3}$$

$$\text{LE} = \left(\frac{0.622 \rho_{\text{air}}}{P_0} \right) L_{\text{v}} A u \left(e_{\text{air}} - e_{\text{s}} \right) \tag{4}$$

where

$$A = \frac{k_{\text{vk}}^2}{\ln\left(\frac{z}{z_0}\right) \ln\left(\frac{z}{z_0}\right)} \tag{5}$$

$$e_{\text{S}} = \text{RH} * 611 \exp\left(\frac{-L_{\text{v}}}{R} \left(\frac{1}{T_{10\,\text{cm}}} - \frac{1}{273.15} \right) \right) \tag{6}$$

where ρ_{air} is the density of air ($1.29\,\text{kg}\,\text{m}^{-3}$), P is the atmospheric pressure computed using the barometric pressure formula, P_0 is the atmospheric pressure at sea level (101 325 Pa), c is the specific heat capacity of air ($1010\,\text{J}\,\text{kg}^{-1}\,\text{K}^{-1}$), A is the dimensionless transfer coefficient, u is the wind speed at Pyramid Station, T_{air} is the air temperature two meters above the surface calculated using a lapse rate of $0.0065\,\text{K}\,\text{m}^{-1}$, L_{v} is the latent heat of vaporization of water ($2.49 \times 10^6\,\text{J}\,\text{kg}^{-1}\,\text{K}^{-1}$), e_{air} is the vapor pressure two meters above the surface, e_{s} is the surface vapor pressure, k_{vk} is Von Karman's constant (0.41), z is the height of meteorological measurements (2 m), z_0 is the surface roughness length, RH is the relative humidity at Pyramid Station, R is the gas constant ($461\,\text{J}\,\text{kg}^{-1}\,\text{K}^{-1}$), and $T_{10\,\text{cm}}$ is the temperature 10 cm below the surface (K). The temperature 10 cm below the surface was used because it is the depth at which the debris transitions from being dry to wet based on results from the thermal conductivity, which will be discussed later. $T_{10\,\text{cm}}$ was approximated by the average

TCD
8, 887–918, 2014

slope in the temperature profiles in the upper 10 cm of the debris. The surface roughness length was assumed to be 0.016 m, which was the surface roughness length measured on a different debris-covered glacier, Miage Glacier, by Brock et al. (2010).

The ground heat flux is different for the linear and the nonlinear models

$$\text{Linear Model: } Q_c = \frac{(T_s - 273.15)}{\text{TR}} \tag{7}$$

$$\text{Nonlinear Model: } Q_c = G_{\text{ratio}} \frac{(T_s - 273.15)}{\text{TR}} \tag{8}$$

where TR is the thermal resistance ($m^2 K^{-1} W^{-1}$), and G_{ratio} is the nonlinear correction factor. The linear model assumes the temperature gradient in the debris is linear from the surface temperature to the debris/ice interface, which is assumed to be at 273.15 K. At the time that Landsat7 images are acquired (10:15 LT), this linear assumption is not accurate (Fig. 3). G_{ratio} is used to approximate the nonlinear temperature gradient in the debris by assuming the temperature gradient in the top 10 cm of the debris is linear. This is a more reasonable assumption (Fig. 3). G_{ratio} is therefore defined as the ratio of the nonlinear temperature gradient to the linear temperature gradient

$$G_{\text{ratio}} = \frac{-k\frac{(T_S - T_{10\,\text{cm}})}{10}}{-k\frac{(T_S - 273.15)}{d}} = \frac{(T_S - T_{10\,\text{cm}})}{(T_S - 273.15)} \cdot \frac{d}{10} \tag{9}$$

where d is the debris thickness (cm). As the Landsat7 images are acquired at 10:15 and the thermistors recorded hourly temperatures, the temperatures in the debris at 10:15 were computed by linearly interpolating between 10:00 and 11:00. These interpolated temperatures were used to compute G_{ratio}.

TCD
8, 887–918, 2014

4 Field results

4.1 Thermal conductivity

The effective thermal conductivity, k, of the debris cover was computed following the methods in Conway and Rasmussen (2000) assuming a density (ρ = 2700 kg m^{-3}) and a specific heat capacity (c = 750 J kg^{-1} K^{-1}) of rock. The average effective thermal conductivity was calculated to be 0.96 (±0.33) W m^{-1} K^{-1}. This effective thermal conductivity agrees well with other thermal conductivities computed in this area, which range from 0.85 to 1.29 W m^{-1} K^{-1} (Conway and Rasmussen, 2000; Nicholson and Benn, 2012). The thermal conductivity was greatly influenced by depth as the average values above and below 10 cm were 0.60 and 1.20 W m^{-1} K^{-1}, respectively.

The drastic difference in thermal conductivity above and below 10 cm is likely due to the amount of water content in the debris. Nicholson and Benn (2006) found the thermal conductivity of wet debris (assuming the pores were saturated with water) to be two to three times larger than dry debris. These results indicate that the top 10 cm of the debris is dry, while 15 cm and lower is wet. This is consistent with observations in the field. These results lend confidence to the use of $T_{10\,\mathrm{cm}}$ for computing the vapor pressure at the surface of the debris as the thermal conductivities indicate the interface of dry and wet debris is between 10 and 15 cm.

4.2 Debris thickness and thermal resistance

The debris thickness in this melt basin ranged from bare ice (0 cm) to depths greater than 1 m. The average debris thickness, assuming a maximum thickness of 1 m, was 42 (±29) cm. These debris thicknesses are consistent with the debris thickness of other debris-covered glaciers in the Everest region (Nakawo et al., 1986; Nicholson and Benn, 2012). Debris thicknesses greater than 1 m were found in the bottom of these melt basins where the debris had likely accumulated over time due to differential melting and backwasting of the debris cover. Areas of thin debris cover were located on

TCD
8, 887–918, 2014

the slopes of the melt basin. These trends were also found at the 12 other sites outside of the melt basin and are identical to those found by Nicholson and Benn (2012). There did not appear to be any trends in debris thickness with respect to aspect.

The thermal resistance, TR, was calculated by dividing the debris thickness, d, by the effective thermal conductivity, k. The thermal resistances in the melt basin range from 0 to 1.04 $m^2 K W^{-1}$ with an average of 0.44 (±0.30) $m^2 K W^{-1}$. Ideally, debris thickness would be sampled over the entire debris-covered glacier along with measurements of the thermal conductivity to derive a thermal resistance map that could be used to validate the modeled thermal resistances. As this was not feasible due to restraints on time and labor, the modeled results within this melt basin and the adjacent cells will constitute the focus area of the satellite imagery that will be compared to the measured thermal resistances to assess the validity of the modeled results.

4.3 Nonlinear correction factor, G_{ratio}

G_{ratio} was computed from all the temperature profiles based on the interpolated temperatures at 10:15. Figure 4 shows the temperature profiles at site LT3 and a schematic of the temperature gradients used to compute G_{ratio}. The average value of G_{ratio} for the melt basin was 2.66 (±0.45). Nicholson (2005) is the only other study that has measured temperature profiles in the Everest area with a small enough spacing between thermistors to compute G_{ratio}. The value of G_{ratio} derived from their temperature profile was 2.55. Based on these results, it appears that the derived value of G_{ratio} on Lhotse Shar/Imja glacier may be transferable to other debris-covered glaciers in the Everest region. However, this should be verified in future studies.

TCD
8, 887–918, 2014

5 Modeled results

5.1 Nonlinear vs. linear model

The nonlinear model accounts for the nonlinear temperature gradient in the debris cover using the G_{ratio} correction factor. Figure 5a and b show the modeled thermal resistance maps for the nonlinear and linear models. For both models, the thermal resistance is greater on the terminal moraine and directly behind Imja Lake and becomes smaller upglacier. These trends indicate thicker debris on the moraine and thinner debris upglacier, which agrees well with debris-covered thickness surveys performed on the Khumbu glacier (Nakawo et al., 1986) and Ngozumpa glacier (Nicholson and Benn, 2012). While the trends are apparent in both models, the linear model derives significantly smaller thermal resistances. In the focus area, the average thermal resistance is 0.41 (±0.23) and 0.15 (±0.09) $m^2 K W^{-1}$ for the nonlinear and linear models, respectively. The nonlinear model agrees very well with the measured thermal resistances, while the linear model severely underestimates the thermal resistances.

One limitation associated with these models is that steep north and west facing pixels are undefined, which means the derived thermal resistances are negative. In the focus area, four pixels are undefined. Table 2 shows that steep slopes on average have a lower value of net radiation due to the topographic correction. Pixels with north and west aspects also have a lower value of net radiation. The topographic correction reduces the amount of incoming shortwave radiation on steeper slopes as well as north and west facing slopes. This reduces the net radiation, which lowers the net energy flux (net radiation and turbulent heat fluxes) used to derive the thermal resistance. In some cases, the net energy flux is negative, which causes a pixel to be undefined. Otherwise, the net energy flux is positive, but small, which results in large thermal resistances. A minimum threshold for the net energy flux of 10 $W m^{-2}$ was set, such that unrealistically high thermal resistances would be classified as undefined.

Table 2 clearly shows that the topographic correction causes a trend in the thermal resistance with respect to slope, with steeper slopes having higher thermal resistances.

TCD
8, 887–918, 2014

This is the opposite trend with respect to slope that was observed in the field. There is also a clear trend with respect to aspect, with north and west facing slopes having higher thermal resistances. This trend was not observed in the field. Therefore, despite the magnitude of thermal resistances agreeing well with the measured values, the model is incapable of capturing the fine local variations.

Derived thermal resistances do not capture local variations with respect to slope and aspect due to the poor resolution of the thermal band. The thermal band has a resolution of 60 m, which causes the surface temperatures over the 60 m pixel to be combined. This is referred to as the mixed-pixel effect. Conventionally, the mixed-pixel effect has been used to explain how bare ice faces reduce the surface temperature of the pixel causing the derived thermal resistances to be low. While this may be true, the mixed-pixel effect also explains how local variations in surface temperature are not properly accounted for. Table 2 reveals that the average surface temperature in the focus area is almost constant and does not vary with respect to slope or aspect. A higher resolution thermal band would show higher surface temperatures on south and east facing slopes, since their orientation allows them to receive more incoming shortwave radiation throughout the morning. North and west facing slopes that do not receive radiation would have lower surface temperatures, which would reduce the thermal resistance. The mixed-pixel effect explains why the modeled results agree well with the average measured values, but do not capture the local variations. Therefore, after the thermal resistance maps have been derived, they must be resampled to 60 m since this is the level of their accuracy.

5.2 Sloped vs. flat model

One method to fill in the undefined pixels from the sloped model is by using the flat model (Foster et al., 2012). Figure 5a and c show the thermal resistance maps derived from the nonlinear sloped and flat models. The flat model captures the trends of higher thermal resistances in the terminal moraine and directly behind the glacier with smaller thermal resistances upglacier. However, these trends are not as prominent as in the

TCD
8, 887–918, 2014

sloped model. The focus area reveals the flat model slightly underestimates the thermal resistances on the glacier as it has an average value of 0.34 (±0.10) $m^2 KW^{-1}$. Table 2 reveals that the thermal resistances are underestimated due to the net radiation being overestimated since the flat model does not correct for topography. This is important because if the flat model values are used to fill in the undefined pixels in the sloped model, one must understand that the thermal resistances will be lower. Furthermore, the main discrepancy between the sloped model and the flat model arises for steep north and west facing slopes, which are the pixels that are classified as undefined. A preferable alternative may be to use the average thermal resistance from the sloped model in Table 2 based on its slope and aspect. When this alternative is performed on the focus area (Fig. 5d), the average thermal resistance for the nonlinear sloped model changes slightly to 0.41 (±0.24) $m^2 KW^{-1}$.

5.3 High resolution vs. poor resolution DEM

The requirement of a high resolution DEM limits the ability to transfer these models to other regions where this may not be available. The ASTER GDEM was used to assess the importance of DEM resolution. The average thermal resistance in the focus area derived using the ASTER GDEM was 0.36 (±0.16) $m^2 KW^{-1}$. These thermal resistances underestimate the measured values and those derived using the DEM generated from ALOS PRISM (Lamsal et al., 2011). However, these thermal resistances are slightly better than those derived from the flat model despite its poorer resolution. Therefore, while a high-resolution DEM will yield better results, we recommend the ASTER GDEM should be used instead of using a flat model to get an estimate of the thermal resistances in an unknown area.

5.4 Thermal resistances for all glaciers in the Everest region

The ASTER GDEM was used to derive the thermal resistances for the debris-covered glaciers in the Everest region (Fig. 6). The Ngozumpa and Khumbu glaciers have

TCD
8, 887–918, 2014

been outlined using the Global Land Ice Measurements from Space (GLIMS) database to compare the derived thermal resistances with previous debris thickness measurements (Nakawo et al., 1986; Nicholson and Benn, 2012). The results on the Khumbu glacier show good agreement with the debris thickness map generated by Nakawo et al. (1986). The thermal resistance is higher towards the terminal moraine and decreases upglacier. The same trend applies on Ngozumpa glacier, which agrees with the debris thickness measurements by Nicholson and Benn (2012). Thermal resistances on both glaciers range from above 0.50 $m^2 K W^{-1}$ near the terminal moraines to less than 0.20 $m^2 K W^{-1}$ upglacier.

5.5 Sensitivity analysis

The model developed in this study relies heavily upon meteorological inputs and assumed values for parameters associated with the debris cover. The meteorological inputs are subject to instrument error and may not be directly transferable from the site of the automatic weather station to the debris-covered glaciers. The particular meteorological parameters of interest are wind speed (u) and air temperature (T_{air}). The parameters associated with the debris cover that may affect results are the surface roughness length (Z_0) and the albedo (α). In addition, there is uncertainty associated with the nonlinear correction factor (G_{ratio}). Lastly, the scenarios of assuming zero latent heat flux (LE) or calculating the latent heat flux (LE) as a function of surface temperature are analyzed. A sensitivity analysis with respect to these parameters and scenarios was performed on the focus area to identify those that affect the derived thermal resistances (TR) the most.

With respect to meteorological and debris cover parameters, the model is most sensitive to the wind speed and albedo and is moderately sensitive to the surface temperature, the nonlinear correction factor, air temperature, and lower values of the surface roughness length (Table 3). The model's sensitivity to wind speed is concerning because the automatic weather station is located 10 km away from the glacier. The model assumes the wind is the same on the glacier as it is at the automatic weather station,

TCD
8, 887–918, 2014

but no data on this exists. Future research should determine if the wind speed at the automatic weather station is representative of the wind speed on the glacier. However, the derived thermal resistances are the average of 12 Landsat7 images, which should account for variations in the meteorological conditions at the automatic weather station and on the glacier.

The assumption of a constant albedo over the debris-covered glacier is another limitation of this model, especially since the model is sensitive to albedo. Methods exist to use other Landsat7 bands to estimate albedo (Liang, 2001); however, the authors had no way of validating these results. Furthermore, since the albedo affects the amount of incoming shortwave radiation absorbed by the debris, higher surface temperatures would likely indicate any large differences in the albedo. The lack of variation in surface temperatures over the debris-covered glacier suggests that assuming a constant albedo is reasonable. Therefore, the average value of albedo of 0.30 determined by a previous study on Ngozumpa glacier (Nicholson and Benn, 2012) was used in this study. Future work should explore deriving the albedo from satellite imagery in conjunction with field measurements to validate these results.

The model was most sensitive to how the latent heat flux term was defined. Previous results have assumed the latent heat flux to be zero based on the assumption that the debris cover is dry (Nakawo and Young, 1982; Foster et al., 2012). The sensitivity analysis reveals that assuming the latent heat flux is zero greatly underestimates the thermal resistance. The problem with this assumption is that the latent heat flux associated with the bare ice faces and melt ponds, which exist throughout the debris cover, is not accounted for. Ideally, the ice faces and melt ponds could be identified from satellite imagery and the latent heat flux could be applied to these pixels, but the resolution of the satellite imagery is too coarse. Other studies have calculated the latent heat flux as a function of the surface temperature (Nakawo and Young, 1982; Nakawo et al., 1999; Nicholson and Benn, 2006; Zhang et al., 2011). The sensitivity analysis shows this assumption greatly overestimates the thermal resistance. This is likely due to the surface vapor pressure in the latent heat flux term being overestimated by the assumption

TCD
8, 887–918, 2014

that the surface vapor pressure is saturated, which is not the case at the time of day when the satellite image is acquired. This study calculates the surface vapor pressure as a function of $T_{10\,cm}$, which results in accurate thermal resistances and reasonable values for the latent heat flux term (results not shown). The use of $T_{10\,cm}$ is supported by the thermal conductivity results, which indicate the debris cover changes from dry to wet between 10 and 15 cm. Conceptually, the use of $T_{10\,cm}$ calculates the latent heat flux associated with the water content in the debris at the wet/dry interface evaporating. The assumption that the latent heat flux may accurately be estimated using $T_{10\,cm}$ is another limitation of this work. However, the thermal resistance, latent heat flux, and thermal conductivity results appear to justify its use in this study. Future work should seek to measure the vapor pressure and water content throughout the debris cover to accurately estimate the latent heat flux.

6 Conclusions

The model described in this paper allows thermal resistances on debris-covered glaciers to be derived from Landsat7 satellite imagery in conjunction with meteorological data from a nearby automatic weather station. The model was applied to glaciers in the Everest region and the resulting thermal resistances were validated with field measurements. The model accounts for the nonlinear temperature gradient in the debris through the use of a nonlinear correction factor. Furthermore, the use of a high resolution DEM greatly improves the results of the derived thermal resistances. In the event that a high resolution DEM is not available, the authors recommend using a lower resolution global DEM to estimate thermal resistances as opposed to using a flat model. A sensitivity analysis reveals that the model is very sensitive to the latent heat flux. This model uses $T_{10\,cm}$ to estimate the latent heat flux, which yields accurate results. Field measurements of the latent heat flux over debris-covered glaciers in this region would allow these estimates to be properly validated. With regards to the meteorological and debris cover parameters, the model is most sensitive to the wind speed and

TCD
8, 887–918, 2014

the surface albedo. Future work should explore how the wind speed varies spatially and derive the albedo from satellite imagery. The main limitation of this work is the poor resolution of the Landsat7 thermal band. The derived thermal resistances must be resampled to the resolution of the thermal band before they are used in melt models or other applications.

Acknowledgements. The authors acknowledge the support of the USAID Climate Change Resilient Development (CCRD) project for the support of Rounce. The meteorological data from Pyramid Station used in this study was collected within the SHARE Project thanks to contributions from the Italian National Research Council and the Italian Ministry of Foreign Affairs. We also acknowledge the support of D. Regmi of Himalayan Research Expeditions for logistical support during fieldwork and D. Lamsal for providing us with a digital elevation model of the Imja Glacial Lake and glacier area. The comments of D. I. Benn and L. Nicholson are greatly appreciated.

References

Barsi, J. A., Schott, J. R., Palluconi, F. D., Helder, D. L., Hook, S. J., Markham, B. L., Chander, G., and O'Donnell, E. M.: Landsat TM and ETM+ thermal band calibration, Can. J. Remote Sens., 29, 141–153, 2003.

Benn, D. I., Bolch, T., Hands, K., Gulley, J., Luckman, A., Nicholson, L. I., Quincey, D., Thompson, S., Toumi, R., and Wiseman, S.: Response of debris-covered glaciers in the Mount Everest region to recent warming, and implications for outburst flood hazards, Earth-Sci. Rev., 114, 156–174, 2012.

Brock, B. W., Mihalcea, C., Kirkbride, M. P., Diolaiuti, G., Cutler, M. E. J., and and Smiraglia, C.: Meteorology and surface energy fluxes in the 2005–2007 ablation seasons at the Miage debris-covered glacier, Mont Blanc Massif, Italian Alps, J. Geophys. Res., 115, D09106, doi:10.1029/2009JD013224, 2010.

Coll, C., Galve, J. M., Sanchez, J. M., and Caselles, V.: Validation of Landsat-7/ETM+ thermal-band calibration and atmospheric correction with ground-based measurements, IEEE T. Geosci. Remote, 48, 547–555, 2010.

TCD
8, 887–918, 2014

Coll, C., Caselles, V., Valor, E., and Niclos, R.: Comparison between different sources of atmospheric profiles for land surface temperature retrieval from single channel thermal infrared data, Remote Sens. Environ., 117, 199–210, 2012.
Conway, H. and Rasmussen, L. A.: Summer temperature profiles within supraglacial debris on Khumbu Glacier, Nepal, debris-covered glaciers, in: Proceedings of a Workshop held at Seattle, Washington, USA, September 2000, 89–97, 2000.
Foster, L. A., Brock, B. W., Cutler, M. E. J., and Diotri, F.: Instruments and methods: a physically based method for estimating supraglacial debris thickness from thermal band remote-sensing data, J. Glaciol., 58, 677–691, 2012.
Fujisada, H., Bailey, G., Kelly, G., Hara, S., and Abrams, M.: ASTER DEM performance, IEEE T. Geosci. Remote, 43, 2707–2714, 2005.
Han, H., Ding, Y., and Liu, S.: A simple model to estimate ice ablation under a thick debris layer, J. Glaciol., 52, 528–536, 2006.
Hock, R. and Noetzli, C.: Areal melt and discharge modelling of Storglaciaren, Sweden, Ann. Glaciol., 24, 211–216, 1997.
Inoue, J. and Yoshida, M.: Ablation and heat exchange over the Khumbu Glacier, Seppyo, 41, 26–31, 1980.
Kayastha, R. B., Takeuchi, Y., Nakawo, M., and Ageta, Y.: Practical prediction of ice melting beneath various thickness of debris cover on Khumbu Glacier, Nepal, using a positive degree-day factor, Int. Assoc. Hydrol. Sci. Publ., 264, 71–81, 2000.
Lamsal, D., Takanobu, S., and Watanabe, T.: Digital terrain modelling using Corona and ALOS PRISM data to investigate the distal part of Imja Glacier, Khumbu Himal, Nepal, J. Mt. Sci., 8, 390–402, 2011.
Liang, S.: Narrowband to broadband conversions of land surface albedo I Algorithms, Remote Sens. Environ., 76, 213–238, 2001.
Mattson, L. E., Gardner, J. S., and Young, G. J.: Ablation on debris covered glaciers: an example from the Rakhiot Glacier, Punjab, Himalaya, Int. Assos. Hydrol. Sci. Publ., 218, 289–296, 1993.
METI/NASA/USGS: ASTER Global DEM Validation Summary Report, Tech. rep., METI/ERSDAC, NASA/LPDAAC, USGS/EROS, 2009.
Mihalcea, C., Brock, B. W., Diolaiuti, G., D'Agata, C., Citterio, M., Kirkbride, M. P., Cutler, M. E. J., and Smiraglia, C.: Using ASTER satellite and ground-based surface temperature

TCD
8, 887–918, 2014

measurements to derive supraglacial debris cover and thickness patterns on Miage Glacier (Mont Blanc Massif, Italy), Cold Reg. Sci. Technol., 52, 341–354, 2008a.
Mihalcea, C., Mayer, C., Diolaiuti, G., D'Agata, C., Smiraglia, C., Lambrecht, A., Vuillermoz, E., and Tartari, G.: Spatial distribution of debris thickness and melting from remote-sensing and meteorological data, at debris-covered Baltoro glacier, Karakoram, Pakistan, Ann. Glaciol., 48, 49–57, 2008b.
Nakawo, M. and Rana, B.: Estimate of ablation rate of glacier ice under a supraglacial debris layer, Geogr. Ann. A, 81, 695–701, 1999.
Nakawo, M. and Young, G. J.: Field experiments to determine the effect of a debris layer on ablation of glacier ice, Ann. Glaciol., 2, 85–91, 1981.
Nakawo, M. and Young, G. J.: Estimate of glacier ablation under a debris layer from surface temperature and meteorological variables, J. Glaciol., 28, 29–34, 1982.
Nakawo, M., Iwata, S. Watanabe, O., and Yoshida, M.: Processes which distribute supraglacial debris on the Khumbu Glacier, Nepal Himalaya, Ann. Glaciol., 8, 129–131, 1986.
Nakawo, M., Yabuki, H., and Sakai, A.: Characteristics of Khumbu Glacier, Nepal Himalaya: recent change in the debris-covered area, Ann. Glaciol., 28, 118–122, 1999.
NASA – National Aeronautics and Space Administration: Landsat 7 Science Data Users Handbook, available at: http://landsathandbook.gsfc.nasa.gov (last access: January 2011), 2011.
NASA Land Processes Distributed Active Archive Center (LP DAAC): ASTER GDEM and Landsat7 ETM+ Level 1T Product, USGS/Earth Resources Observation and Science (EROS) Center, Siox Falls, South Dakota, 2011.
Nicholson, L. I.: Modelling Melt Beneath Supraglacial Debris: Implications for the Climatic Response of Debris-Covered Glaciers, PhD Thesis, University of St Andrews, UK, 2005.
Nicholson, L. and Benn, D. I.: Calculating ice melt beneath a debris layer using meteorological data, J. Glaciol., 52, 463–470, 2006.
Nicholson, L. and Benn, D. I.: Properties of natural supraglacial debris in relation to modelling sub-debris ice ablation, Earth Surf. Proc. Land., 38, 490–501, 2012.
Nuth, C. and Kääb, A.: Co-registration and bias corrections of satellite elevation data sets for quantifying glacier thickness change, The Cryosphere, 5, 271–290, doi:10.5194/tc-5-271-2011, 2011.
Östrem, G.: Ice melting under a thin layer of moraine, and the existence of ice cores in moraine ridges, Geogr. Ann., 41, 228–230, 1959.

TCD
8, 887–918, 2014

Reid, T. D. and Brock, B. W.: An energy-balance model for debris-covered glaciers including heat conduction through the debris layer, J. Glaciol., 56, 903–916, 2010.

Reid, T. D., Carenzo, M., Pellicciotti, F., and Brock, B. W.: Including debris cover effects in a distributed model of glacier ablation, J. Geophys. Res., 117, D18105, doi:10.1029/2012JD017795, 2012.

Suzuki, R., Fujita, K., and Ageta, Y.: Spatial distribution of thermal properties on debris-covered glaciers in the Himalayas derived from ASTER data, Bulletin of Glaciological Research, 24, 13–22, 2007.

Takeuchi, Y., Kayastha, R. B., and Nakawo, M.: Characteristics of ablation and heat balance in debris-free and debris-covered areas on Khumbu Glacier, Nepal Himalayas, in the premonsoon season, Int. Assoc. Hydrol. Sci. Publ., 264, 53–61, 2000.

Zhang, Y., Fujita, K., Liu, S., Liu, Q., and Nuimura, T.: Distribution of debris thickness and its effect on ice melt at hailuogou glacier, southeastern Tibetan Plateau, using in situ surveys and ASTER imagery, J. Glaciol., 57, 1147–1157, 2011.

TCD
8, 887–918, 2014

Table 1. Overview of satellite imagery used in this study.

Satellite	Year	Date	Purpose	Resolution (m)
Landsat 7	2002	4 Oct	Ts	60
Landsat 7	2003	16 May	Ts	60
Landsat 7	2004	7 Sep	Ts	60
Landsat 7	2004	9 Oct	Ts	60
Landsat 7	2005	21 May	Ts	60
Landsat 7	2005	12 Oct	Ts	60
Landsat 7	2007	27 May	Ts	60
Landsat 7	2007	28 Jun	Ts	60
Landsat 7	2007	2 Oct	Ts	60
Landsat 7	2008	29 May	Ts	60
Landsat 7	2008	2 Sep	Ts	60
Landsat 7	2009	17 Jun	Ts	60
ALOS PRISM	2006	4 Dec	DEM	2.5
ASTER	2000–2008		DEM	15–50

TCD
8, 887–918, 2014

Table 2. Trends in thermal resistance, surface temperature, and net radiation with respect to slope and aspect in the focus area.

Topographic Parameter		Sloped Model			Flat Model		
		Avg TR ($m^2 KW^{-1}$)	Avg Ts (K)	Avg Rn ($W m^{-2}$)	Avg TR ($m^2 KW^{-1}$)	Avg Ts (K)	Avg Rn ($W m^{-2}$)
Slope	0–5	0.34	290.44	521	0.32	290.44	526
	5–10	0.38	290.33	504	0.34	290.33	528
	10–20	0.38	290.33	472	0.35	290.32	527
	20–30	0.49	290.47	422	0.36	290.47	526
	> 30	0.82	290.53	300	0.38	290.47	528
Aspect	N	0.46	290.38	479	0.36	290.38	528
	W	0.45	290.36	428	0.34	290.35	527
	S	0.31	290.31	507	0.32	290.31	527
	E	0.29	290.53	560	0.37	290.53	526

TCD
8, 887–918, 2014

Table 3. Sensitivity analysis for select meteorological and model parameters.

	T_S	G_{ratio}	T_{air}	u	z_0	α	LE	TR avg	Change
Baseline	–	2.66	AWS	AWS	0.016	0.30	$f(T_{10})$	0.41	–
T_S	+1	–	–	–	–	–	–	0.46	+0.06
	−1	–	–	–	–	–	–	0.34	−0.07
G_{ratio}	–	+0.45	–	–	–	–	–	0.48	+0.07
	–	−0.45	–	–	–	–	–	0.34	−0.07
T_{air}	–	–	+2	–	–	–	–	0.34	−0.07
	–	–	−2	–	–	–	–	0.45	+0.04
u	–	–	–	+1	–	–	–	0.53	**+0.12**
	–	–	–	−1	–	–	–	0.29	**−0.12**
z_0	–	–	–	–	0.010	–	–	0.35	−0.06
	–	–	–	–	0.022	–	–	0.42	+0.01
α	–	–	–	–	–	0.20	–	0.3	**−0.11**
LE	–	–	–	–	–	–	$f(T_S)$	0.69	**+0.28**
	–	–	–	–	–	–	zero	0.26	**−0.11**

TCD
8, 887–918, 2014

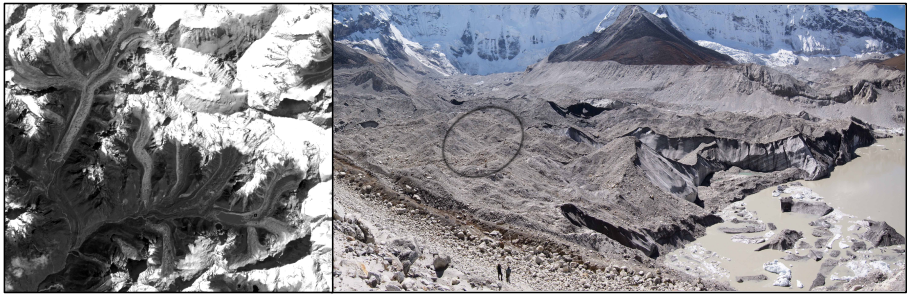

Fig. 1. (Left) Panchromatic band from Landsat7 from 4 October 2002 showing Imja Lake amongst debris-covered glaciers in Everest region; (right) debris-covered glacier behind Imja Lake with the melt basin identified.

TCD
8, 887–918, 2014

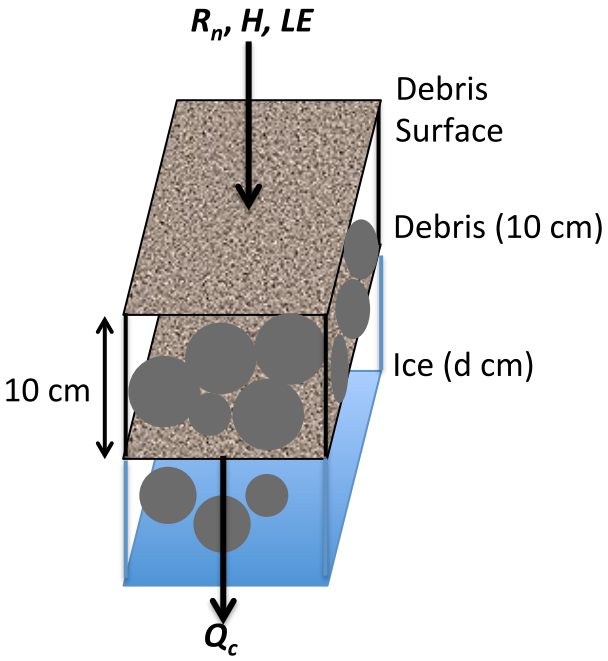

Fig. 2. Control volume of surface energy balance model.

TCD
8, 887–918, 2014

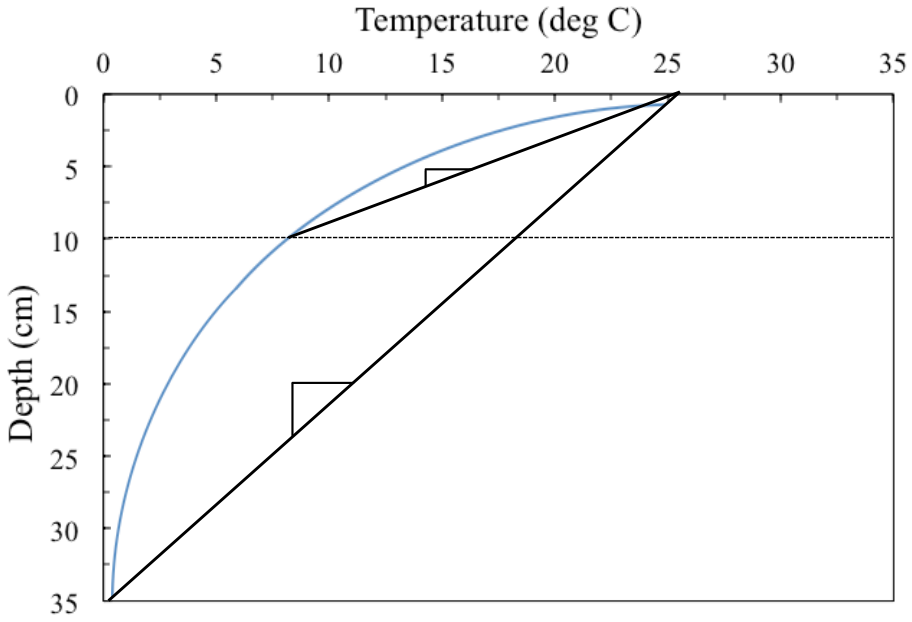

Fig. 3. Conceptual temperature profile showing gradients used to compute G_{ratio}.

TCD
8, 887–918, 2014

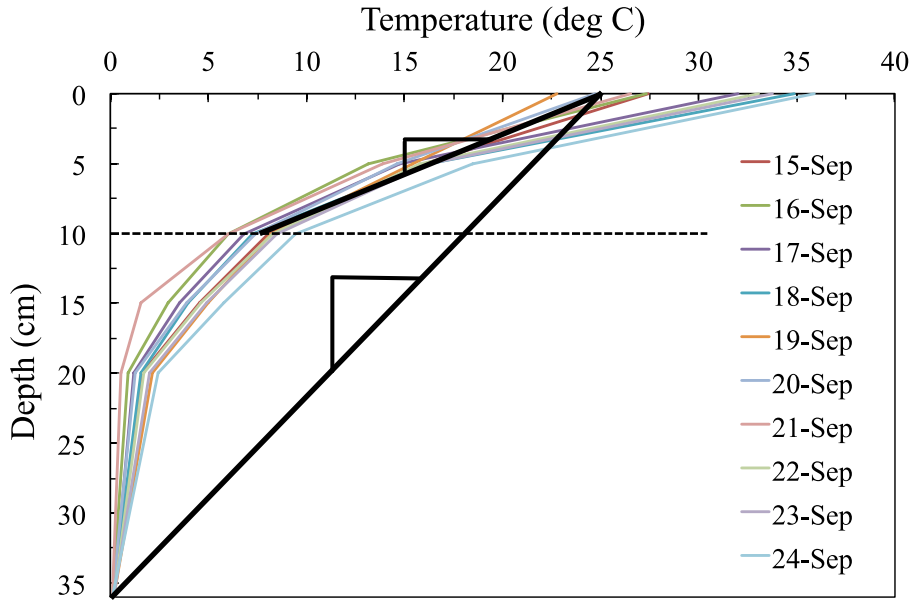

Fig. 4. Temperature profiles at site LT3 at 10:15 with the temperature gradients used to compute G_{ratio} identified.

TCD
8, 887–918, 2014

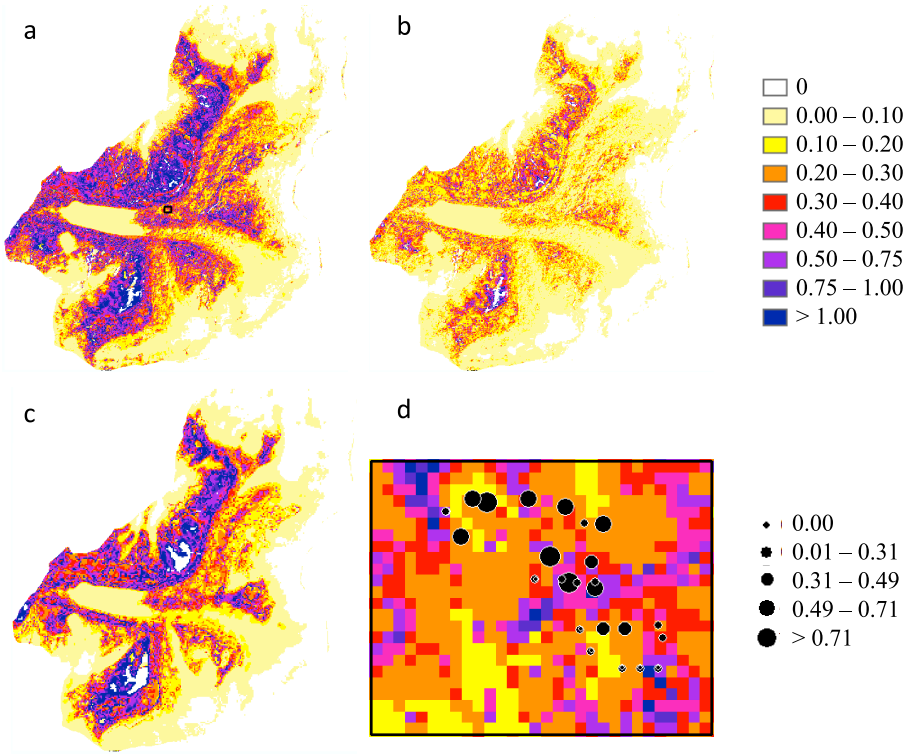

Fig. 5. Thermal resistances derived from **(a)** nonlinear sloped model with a box showing the focus area, **(b)** linear sloped model, **(c)** nonlinear flat model, and **(d)** focus area with undefined pixels replaced and measured debris thickness displayed.

TCD
8, 887–918, 2014

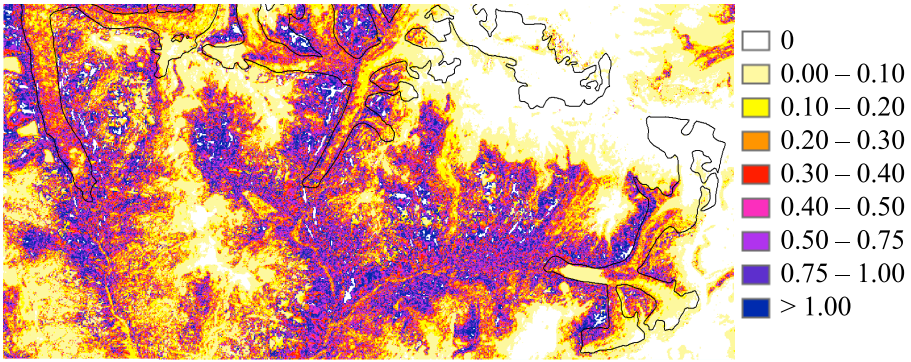

Fig. 6. Thermal Resistances for debris-covered glaciers in Everest region with Lhotse Shar/Imja, Khumbu, and Ngozumpa glaciers roughly outlined using GLIMS outlines.

TCD
8, 887–918, 2014